The ^{136}Xe +^{198} Pt reaction: a detailed re-examination

V. V. Desai[1], W. Loveland[1,a], R. Yanez[1], G. Lane[2], S. Zhu[3,5], A. D. Ayangekaa[4,5], J. P. Greene[5], F. G. Kondev[5], R. V. F. Janssens[6,7], P. A. Copp[8]

[1] Department of Chemistry, Oregon State University, Corvallis, OR 97331, USA
[2] Department of Nuclear Physics, Australian National University, Canberra, ACT 2601, Australia
[3] National Nuclear Data Center, Brookhaven National Laboratory, Upton, NY 11973, USA
[4] U.S. Naval Academy, Annapolis, MD 21402, USA
[5] Physics Division, Argonne National Laboratory, Argonne, IL 60439, USA
[6] Department of Physics and Astronomy, University of North Carolina at Chapel Hill, Chapel, NC 27599, USA
[7] Triangle Universities Nuclear Laboratory, Duke University, Durham, NC 27708, USA
[8] Department of Physics, University of Massachusetts Lowell, Lowell, MA 01854, USA

Received: 2 February 2020 / Accepted: 29 April 2020 / Published online: 25 May 2020

Communicated by Alexandre Obertelli

Abstract We extend previous measurements of the transfer product yields in the reaction of $E_{c.m.} = 450$ MeV ^{136}Xe with ^{198}Pt by measurements of the product yields using Gammasphere. By recording events occurring in beam bursts and in between beam bursts, we are able to extend the number of measured product yields from 78 to 171 nuclides. Our new data span a much wider range of Z and A than observed in previous work and when compared to theoretical predictions, these new measurements provide a more stringent and thorough test of models of multi-nucleon transfer (MNT) reactions.

1 Introduction

Multi-nucleon transfer (MNT) reactions are thought to be the preferred way of making neutron-rich heavy nuclei and producing nuclei near the N = 126 shell. From the perspective of heavy element science, it is sobering to realize that all the known nuclei from Fm to Og are neutron-deficient relative to β-stability. (This is not surprising as most of these nuclei are made in fusion-evaporation reactions.) This neutron deficiency means that to access the longer half-lives of the neutron-rich heavy nuclei, one needs to look at MNT reactions or other synthetic paths.

There has been considerable activity in the investigation of the use of MNT reactions to make new n-rich heavy nuclei and nuclei near the N=126 shell. Three recent review articles summarize much of this effort [1–3]. There are basically four theoretical approaches to describing these reactions. The first of these is the semi-classical model of Winther and Pollorollo [4–6], GRAZING. GRAZING uses a semi-classical model of the reacting ions moving on classical trajectories with quantum calculations of the probability of excitation of collective states and of nucleon transfer. This model describes few nucleon transfers [7] well. We use a variant of the GRAZING code, GRAZING-F [8], that is designed to take into account fission decay of the transfer products.

A second, widely used model for product yields in MNT reactions is the di-nuclear systems (DNS) model [9]. The DNS model assumes that the colliding nuclei exchange nucleons or clusters in a touching position. The touching nuclei retain their identity in this process. This model can be used to treat fusion (as the end result of a series of transfers) or quasifission (the fission of the di-nuclear configuration without forming a compound nucleus). Calculation of MNT processes in heavy neutron-rich nuclei using the DNS approach have been presented [10,11].

A third model for predicting product yields in MNT reactions is the improved quantum molecular dynamics model (ImQMD) [12]. Recent applications of this model to MNT reactions have been published [13–16]. The ImQMD model simulates the time evolution of the reacting system, using a mean field part (with a nuclear equation of state) and a collision part involving nucleon-nucleon collision cross sections [12].

A fourth approach uses Langevin model calculations. This type of calculation was used by Zagrebaev and Greiner in their seminal papers on MNT reactions [17,18]. More recently, these calculations have been employed by Karpov

[a] e-mail: lovelanw@onid.orst.edu (corresponding author)

and Saiko [19–21] predict the yields of MNT products in reactions similar to those considered in this paper.

Multi-nucleon transfer processes in the ^{136}Xe $+^{198}$ Pt reaction have the potential to form new heavy n-rich nuclei and nuclei near the N = 126 shell closure [22]. Desai et al. [24] published a survey of the yield of the target-like fragments (TLFs) and projectile-like fragments (PLFs) in this reaction at a center of target beam energy of 760.5 MeV ($E_{c.m.}$ = 450 MeV). These workers detected the fragments by post-irradiation counting of the irradiated target. They detected 42 PLFs and 36 TLFs and compared their results with predictions of the GRAZING., DNS, and ImQMD models, concluding that only the ImQMD model describes the data adequately.

In this paper, we report the results of a study of the $E_{c.m.}$ = 450 MeV ^{136}Xe+^{198}Pt reaction in which we detected, using Gammasphere, the γ -ray decay of the PLFs and TLFs that occurred within the beam bursts and between the beam bursts. As such, this study complements and extends the work of Desai et al. [24].

2 Experimental

2.1 Experimental setup

The experiment took place at the Gammasphere facility of the Argonne National Laboratory. In this run, there were 90 operating Compton-suppressed Ge detectors (out of the possible 100 detectors) in Gammasphere. The experimental method used was similar to that of Barrett [23]. A beam of 860 MeV ^{136}Xe struck a sandwich of a 3.2 mg/cm^2 ^{198}Pt foil, a 4.0 mg/cm^2 ^{198}Pt foil and a 24 mg/cm^2 ^{197}Au stopper foil. The mean beam energy in the Pt foil stack was E_{lab} = 760.5 MeV [25–27] ($E_{c.m.}$ = 451 MeV). After this beam passes thru the two Pt foils , the beam energy was reduced to 678 MeV [25] or E_{cm} = 401.9 MeV which is below the Bass barrier [27] or the interaction barrier for the ^{136}Xe $+^{197}$ Au reaction. Note that, once the energy has dropped past the interaction barrier, no further interactions with the target nuclei will occur. The methods for the energy and efficiency calibration of Gammasphere are described in [26]

The beam intensity was monitored periodically by inserting a suppressed Faraday cup into the beam line in front of the target. The average beam intensity was 3.54 $\times$ 10^8 particle/s. The irradiation lasted 28.3 h. (The irradiation conditions were exactly those of Desai et al. [24]). The spacing between accelerator beam bursts was 824 ns. Triple gamma-ray coincidence events were recorded.

2.2 Data analysis

The analysis of the in-beam Gammasphere data was carried out using the Rad-Ware [28] software. Two γ-γ-γ histograms, called cubes, were constructed. One cube was constructed using prompt gamma decays recorded during the beam burst (IB), and the other included only delayed gamma decays recorded between the beam bursts (OB). Using the program LEVIT8R, the identification of the reaction products was determined by gating on two low-lying gamma transitions in each cube for a given nucleus. The observation of the next higher up transition confirmed the identity of the reaction product and was integrated. This procedure was repeated for all observed three-fold transitions for a given nucleus. The intensities for each three-fold transition were corrected for internal conversion, absolute efficiency, and triple-coincidence efficiency (which was determined using the method outlined in [29,30]). All of the individual transition intensities from both the IB cube and OB cube were summed to give the total gamma yields of each reaction product. Once again, absolute cross sections were determined using equations for growth and decay [31], taking into account the beam intensities.

Following irradiation, gamma-ray spectroscopy of the target radioactivities was carried out using a well-calibrated Ge detector as described by Desai et al. [24]. The resulting independent and cumulative yields of the 78 products detected have been published by Desai et al. [24]. The independent yield of a nuclide is just what it appears, the yield of that nucleus as a primary reaction product. But many of the reaction products are β-emitters and as such their yields integrate the yields of their β-decay precursors. Such yields are referred to as cumulative yields.

As in the radioactive decay analysis, the in-beam and out-of-beam yields of ground state and isomeric states were summed to give a total nuclidic cross section. These measured absolute nuclidic cross sections are the “cumulative” yields for these data and are represented in Tables 1, 2, 3 and 4 along with the results of the previous work [24]. The cross sections are identified as IB and/or OB in Tables 1, 2, 3 and 4 depending on if the cross section was determined by gamma transitions found in the prompt cube of in-beam burst events (IB), or in the delayed cube of out-of-beam burst events (OB), or both. The designation of RD in Tables 1, 2, 3 and 4 indicates nuclei measured in the post-beam studies [24]. The same procedure to determine independent yields in the decay analysis was then applied to these data to determine independent yields in the analysis of the Gammasphere data. These independent yield cross sections are represented in Tables 1, 2, 3 and 4.

How does this paper differ from the previous work of Desai et al. [24]? In this work, we deal with the analysis of the activities detected in each beam burst and in between

Table 1 Projectile-like fragment and fission fragment cumulative and independent yields for ^{136}Xe $+^{198}$ Pt at $E_{cm} = 450$ MeV for cases where the fragment mass is less than the projectile mass

Isotope	σ_{CY} (mb)	σ_{IY} (mb)	Type of yield
^{110}In	1.87 ± 0.02	1.78 ± 0.02	RD
^{115}In^{m}	2.59 ± 0.07	1.79 ± 0.18	RD
^{116}In	0.72 ± 0.05	0.72 ± 0.07	OB
^{117}In	8.18 ± 0.27	4.75 ± 0.48	OB
^{118}In	1.55 ± 0.06	1.04 ± 0.10	OB
^{120}In	2.99 ± 0.09	2.38 ± 0.24	OB
^{122}In	2.49 ± 0.09	2.22 ± 0.22	OB
^{124}In	1.52 ± 0.08	1.43 ± 0.14	OB
^{118}Sn	1.55 ± 0.06	0.54 ± 0.05	OB
^{119}Sn	0.49 ± 0.03	0.21 ± 0.02	OB
^{120}Sn	7.56 ± 0.25	0.12 ± 0.03	OB
^{121}Sn	0.11 ± 0.01	0.067 ± 0.007	OB
^{122}Sn	6.87 ± 0.22	4.72 ± 0.47	OB
^{123}Sn	6.12 ± 0.19	4.61 ± 0.46	OB
^{124}Sn	1.49 ± 0.08	1.22 ± 0.12	OB
^{125}Sn	0.17 ± 0.02	0.17 ± 0.02	OB
^{119}Sb	6.45 ± 0.30	6.08 ± 0.61	OB
^{120}Sb^{m}	0.37± 0.05	0.37± 0.05	RD
^{121}Sb	0.44 ± 0.03	0.17 ± 0.02	OB
^{122}Sb	1.65± 0.03	1.65 ± 0.03	RD
^{123}Sb	1.46 ± 0.05	0.81 ± 0.08	OB
^{126}Sb	1.42 ± 0.21	1.42 ± 0.21	RD
^{127}Sb	1.35 ± 0.07	1.12 ± 0.11	OB, RD
^{128}Sb	1.26 ± 0.06	1.11 ± 0.11	RD, OB
^{129}Sb	1.29 ± 0.06	1.17 ± 0.12	OB
^{130}Sb	2.51 ± 0.09	2.34 ± 0.23	OB
^{124}Te	1.43 ± 0.25	1.43 ± 0.28	IB
^{126}Te	3.08 ± 0.25	1.83 ± 0.18	IB
^{128}Te	33.5 ± 0.3	24.9 ± 2.5	IB
^{130}Te	12.0 ± 0.95	10.2 ± 1.0	RD
^{131}Te^{m}	1.73 ± 0.09	1.13 ± 0.11	OB, RD
^{132}Te	2.31 ± 0.08	2.13 ± 0.2	OB, IB
^{133}Te	3.39 ± 0.12	3.20 ± 0.32	OB
^{134}Te	5.83 ± 0.20	5.83 ± 0.58	OB
^{124}I	1.20 ± 0.05	1.20 ± 0.05	RD
^{130}I	9.78 ± 0.04	9.78 ± 0.98	RD, OB
^{131}I	18.2 ± 0.5	15.3 ± 1.5	RD
^{132}I	3.53 ± 0.10	3.15 ± 0.31	RD, OB
^{133}I	14.2 ± 0.1	10.2 ± 1.0	OB, RD
^{134}I	2.89 ± 0.10	2.27 ± 0.23	OB
^{135}I	4.63 ± 0.42	4.63 ± 0.46	RD

Table 2 Projectile-like fragment cumulative and independent yields for ^{136}Xe $+^{198}$ Pt at $E_{c.m.} = 450$ MeV for cases where the fragment mass is greater or equal to the projectile mass

Isotope	σ_{CY} (mb)	σ_{IY} (mb)	Type of yield
^{125}Xe	0.87 ± 0.5	0.79 ± 0.46	RD
^{127}Xe	6.77 ± 0.39	6.57 ± 0.66	OB, RD
^{130}Xe	8.49 ± 0.79	1.59 ± 0.16	IB
^{132}Xe	17.7 ± 0.6	5.57 ± 0.56	OB
^{133}Xe^{m}	21.3 ± 0.30	13.2 ± 1.3	IB, RD
^{134}Xe	35.2 ± 1.0	16.9 ± 1.7	OB, IB
^{135}Xe	35.9 ± 0.5	22.2 ± 2.2	OB, IB, RD
^{136}Xe	63.22 ± 1.79	41.1 ± 4.1	OB, IB
^{138}Xe	15.8 ± 0.55	15.8 ± 1.6	OB, IB
^{139}Xe	19.1± 0.7	15.9 ± 1.6	OB
^{127}Cs	11.91 ± 0.44	11.0 ± 1.1	RD, OB
^{132}Cs	11.9 ± 0.2	11.9 ± 0.2	RD
^{135}Cs	13.2 ± 0.4	13.2 ± 1.3	OB
^{136}Cs	15.5 ± 0.4	15.5 ± 1.6	RD
^{138}Cs	19.5 ± 0.6	17.6 ± 1.8	OB
^{131}Ba	1.1± 0.2	0.96 ± 0.20	RD
^{132}Ba	1.82± 0.07	0.42± 0.04	IB
^{134}Ba	5.26 ± 0.08	5.26 ± 0.23	OB, IB
^{135}Ba^{m}	12.5 ± 0.2	12.5 ± 0.2	RD
^{136}Ba	8.26 ± 0.62	4.52 ± 0.45	OB, IB
^{138}Ba	6.7 ± 1.1	4.71 ± 0.77	IB
^{139}Ba	3.76 ± 0.12	2.88 ± 0.30	IB, OB
^{140}Ba	11.95 ± 0.01	10.6 ± 1.0	RD
^{141}Ba	3.72± 0.13	3.23± 0.32	OB
^{136}La	1.44 ± 0.10	1.44 ± 0.14	IB
^{139}La	1.39 ± 0.06	1.38 ± 0.14	OB
^{140}La	2.29± 0.06	2.28 ± 0.23	RD
^{142}La	0.21 ± 0.02	0.19 ± 0.02	OB
^{135}Ce	4.41 ± 0.17	3.89 ±0.39	OB
^{136}Ce	1.69 ± 0.09	1.43 ± 0.14	OB
^{138}Ce	3.97 ± 0.14	2.89 ± 0.29	OB
^{140}Ce	6.09 ± 0.20	4.02 ± 0.40	OB
^{142}Ce	1.44± 0.11	1.14 ± 0.11	IB
^{143}Ce	4.21 ± 0.08	3.56 ± 0.36	RD

beam bursts (rather than those measured in post irradiation decay). What do we learn from these new data? A statistical summary of the activities detected in this work and the previous work is shown in Table 5. Not only is the number of detected MNT fragments much larger (171 vs. 78) but the range of the activities is larger, in general. This allows us to make more detailed comparisons between the data and current models of MNT reactions. [Also the addition of more product yields allowed us to redefine the independent yields of nuclei determined from these data. For example, some of

Table 3 Target-like fragment cumulative and independent yields for ^{136}Xe +^{198} Pt at $E_{c.m.} = 450$ MeV for cases where the fragment mass is less than the target mass

Isotope	σ_{CY} (mb)	σ_{IY} (mb)	Type of yield
^{173}Hf	0.72 ± 0.02	0.67 ± 0.07	RD
^{175}Hf	2.51 ± 0.47	2.17 ± 0.41	RD
^{176}Hf	4.259 ± 0.195	3.49 ±0.45	OB
^{177}Hf	4.613 ± 0.467	4.61 ±0.47	OB
^{178}Hf	12.82 ± 0.41	12.8 ± 1.3	OB
^{180}Hf^{m}	0.65 ± 0.22	0.65 ± 0.22	RD
^{180}Hf	10.49 ± 0.35	7.29 ± 0.73	OB
^{181}Hf	5.42 ± 0.18	4.14 ± 0.41	OB
^{182}Hf	1.49 ± 0.05	1.49 ±0.15	OB
^{176}Ta	1.38 ± 1.18	1.21 ± 1.03	RD
^{177}Ta	2.1 ± 1.9	1.8 ± 1.6	RD
^{179}Ta	5.55 ± 0.21	3.96 ± 0.40	OB
^{182}Ta	4.47 ± 0.19	4.47 ±0.45	OB
^{184}Ta	0.82 ± 0.02	0.73 ± 0.07	RD
^{176}W	0.25 ± 0.07	0.24 ± 0.07	IB
^{180}W	14.61 ± 0.85	11.9 ± 1.2	OB, IB
^{182}W	3.39 ± 0.12	2.34 ± 0.23	OB
^{184}W	3.47 ± 0.13	2.43 ± 0.24	OB
^{186}W	5.21 ± 0.19	4.30 ± 0.43	OB
^{180}Re	0.75 ± 0.04	0.69 ± 0.07	OB
^{181}Re	1.73 ± 0.78	1.53 ± 0.69	RD
^{182}Re	8.26 ± 2.38	8.19 ± 2.43	RD
^{183}Re	4.58 ± 0.18	7.6 ± 2.2	OB
^{188}Re	7.77 ± 0.58	7.77 ± 0.78	RD
^{189}Re	17.5 ± 0.9	14.7 ± 1.5	RD
^{190}Re	8.43 ± 0.30	8.43 ± 0.84	OB
^{182}Os	1.01 ± 0.16	0.91 ± 0.15	RD
^{183}Os	0.83 ± 0.04	0.41 ± 0.04	RD
^{186}Os	4.04 ± 0.66	2.77± 0.45	IB
^{188}Os	4.00 ± 0.63	2.09 ± 0.32	IB
^{190}Os	34.4 ± 3.57	11.9 ± 1.2	IB
^{192}Os	35.4 ± 0.47	32.1 ± 3.2	IB
^{188}Ir	4.28 ± 0.94	4.27 ± 0.94	RD
^{190}Ir	3.11 ± 0.03	1.55 ± 0.16	RD
^{194}Ir	3.18 ± 1.25	3.18 ± 1.25	RD
^{195}Ir^{m}	17.8 ± 1.9	17.8 ± 1.9	RD
^{196}Ir	32.23 ± 0.99	22.9 ± 2.2	OB
^{196}Ir^{m}	8.21 ± 0.29	8.21 ± 0.82	OB/RD

Table 4 Target-like fragment cumulative and independent yields for ^{136}Xe +^{198} Pt at $E_{c.m.} = 450$ MeV for cases where the fragment mass is greater or equal to the target mass

Isotope	σ_{CY} (mb)	σ_{IY} (mb)	Type of yield
^{190}Pt	1.36 ± 0.19	1.30 ± 0.18	IB
^{191}Pt	5.6 ± 0.01	5.24 ± 0.52	RD
^{192}Pt	5.39 ± 0.47	4.93 ± 0.49	IB
^{194}Pt	19.17 ± 1.38	16.1 ± 1.6	IB
^{195}Pt^{m}	26.5 ± 5.7	10.6± 2.3	RD
^{196}Pt	59.6 ± 6.7	29.4 ± 3.3	IB
^{198}Pt	77.9 ± 5.5	51.6 ± 5.2	IB
^{200}Pt	10.4 ± 0.8	10.4 ± 1.0	IB
^{192}Au	6.53 ± 0.22	5.65 ± 0.56	OB
^{193}Au	15.4 ± 9.0	13.0 ± 7.6	RD
^{194}Au	6.55 ± 0.10	6.55 ± 0.66	RD, OB
^{195}Au^{m}	3.4 ± 0.1	2.9 ± 0.3	RD
^{196}Au	23.2 ± 0.7	3.34 ± 0.67	OB
^{196}Au^{m}	115.3 ± 0.5	115.3 ± 11.5	RD
^{197}Au	9.56 ± 0.31	6.61 ± 0.66	OB
^{198}Au	17.6 ± 0.3	15.1 ± 1.5	RD
^{199}Au	205.6 ± 0.6	167.6 ± 16.8	RD
^{200}Au	4.62 ± 0.16	2.83 ± 0.28	OB
^{200}Au^{m}	1.79 ± 0.08	1.79 ± 0.18	RD
^{195}Hg^{m}	3.4 ± 0.1	2.65 ± 0.27	RD
^{196}Hg	9.0 ± 0.8	6.48± 0.65	IB
^{197}Hg	6.99 ± 0.78	5.24 ± 0.59	RD
^{198}Hg	2.16 ± 0.43	1.22 ± 0.24	IB
^{199}Hg	4.05 ± 0.15	4.05±0.41	OB
^{200}Hg	5.11 ± 0.24	4.08 ± 0.41	IB
^{202}Hg	1.39 ± 0.35	1.24 ± 0.31	IB
^{203}Hg	1.22 ± 0.06	1.12 ± 0.11	OB, RD
^{206}Hg	1.05± 0.05	1.05± 0.11	OB
^{194}Tl	2.48 ± 0.09	2.31 ± 0.23	OB
^{196}Tl	3.23 ± 0.12	2.80 ± 0.28	OB
^{197}Tl	7.70 ± 0.22	6.25 ± 0.62	IB, OB
^{198}Tl	6.42 ± 0.24	4.78 ± 0.48	OB
^{199}Tl	13.48 ± 0.41	9.40 ± 0.94	IB, OB
^{200}Tl	6.61 ± 0.24	5.09 ± 0.51	RD, OB
^{200}Tl^{m}	8.60 ± 0.29	6.64 ± 0.66	OB
^{201}Tl	13.01 ± 0.37	8.47 ± 0.85	OB, IB, RD
^{202}Tl	5.40 ± 0.22	5.40 ± 0.54	RD, OB
^{203}Tl	3.27 ± 0.15	2.69± 0.27	OB
^{204}Tl	2.23 ± 0.09	2.23 ± 0.22	OB
^{205}Tl	0.337 ± 0.017	0.30 ± 0.03	OB
^{206}Tl	0.022 ± 0.002	0.020 ± 0.002	OB
^{200}Pb	4.7± 0.2	3.8± 0.4	RD
^{201}Pb	4.4 ± 0.2	3.28 ± 0.37	RD,OB

Table 4 continued

Isotope	σ_{CY} (mb)	σ_{IY} (mb)	Type of yield
$^{202}Pb^{m}$	6.2± 0.3	6.2 ± 0.6	RD
^{203}Pb	4.08 ± 0.19	2.80 ± 0.28	IB, RD
^{204}Pb	3.73 ± 0.21	1.85 ± 0.18	IB
^{200}Bi	1.76± 0.07	1.75 ± 0.18	OB
^{204}Bi	0.87 ± 0.02	0.63 ± 0.06	OB, RD
^{206}Bi	0.96 ± 0.05	0.92 ± 0.09	OB
^{207}Bi	0.51 ± 0.03	0.24 ± 0.02	OB
^{208}Bi	0.36 ± 0.03	0.14 ± 0.01	OB
^{207}Po	0.96 ± 0.07	0.96 ± 0.10	OB
^{208}Po	0.47 ± 0.03	0.28 ± 0.04	OB
^{207}At	0.36± 0.02	0.30 ± 0.03	OB
^{208}At	0.53± 0.03	0.42 ± 0.04	OB
^{209}At	0.57 ± 0.03	0.41 ± 0.04	OB
^{210}At	0.42 ± 0.03	0.28 ± 0.03	OB
^{211}At	0.23 ± 0.02	0.16 ± 0.02	OB

Table 5 Summary comparison between this work and that of [24]

Element	Z	Range [24]	Range (this work)	No. Yields [24]	No. yields (this work)
In	49	110–115	110–124	2	8
Sn	50	–	118–125	–	8
Sb	51	120–128	119–130	5	10
Te	52	131	124–134	1	8
I	53	124–135	124–135	6	7
Xe	54	125–135	125–139	4	10
Cs	55	127–136	127–138	3	5
Ba	56	131–140	131–141	3	9
La	57	140	136–142	1	3
Ce	58	143	135-143	1	6
Hf	72	173–180	173–182	3	9
Ta	73	176-184	176–184	3	5
W	74	–	176–186	–	5
Re	75	181–189	180–190	4	7
Os	76	182–183	182–192	2	6
Ir	77	188–196	188–196	5	6
Pt	78	191–195	190–200	2	8
Au	79	193–200	192–200	6	11
Hg	80	195–203	195–206	3	9
Tl	81	200–202	194–206	3	13
Pb	82	200–203	200–204	4	5
Bi	53	204	200-208	1	5
Po	54	–	207–208	–	2
At	85	–	207–211	–	5

Table 6 Summary comparison of the yields of n-rich products in typical fragmentation [33] and MNT reactions. The MNT reactions used in this comparison are $E_{c.m.}$ = 450 MeV $^{136}Xe + ^{208}Pb$ [23] and $E_{c.m.}$ = 450 MeV $^{136}Xe + ^{198}Pt$ (this work)

Z	Fragment	Fragmentation cross section (mb)	N
82	^{207}Pb	120 ± 0.3	125
81	^{207}Tl	21 ± 0.4	126
80	^{206}Hg	0.53 ± 0.10	126
79	^{205}Au	0.012 ± 0.002	126
78	^{204}Pt	0.00027 ± 0.00007	126
Z	Product	MNT cross section (mb) [23]	N
82	^{208}Pb	20.6 ± 4.1	126
81	^{207}Tl	0.13 ± 0.03	126
80	^{206}Hg	0.0093 ± 0.0019	126
79	^{199}Au	6.23 ± 1.25	120
78	^{202}Pt	0.178 ± 0.036	124
Z	Product	MNT cross section (mb) (This work)	N
85	^{211}At	0.16 ± 0.02	126
84	^{208}Po	0.28 ± 0.04	124
83	^{208}Bi	0.14 ± 0.01	125
82	^{204}Pb	1.85 ± 0.18	122
81	^{206}Tl	0.020 ± 0.002	125
80	^{206}Hg	1.05 ± 0.11	126

the independent yields shown in this paper for nuclides that were designated as RD nuclides differ slightly from those given in [24] due to the improved fitting of the charge distributions with the larger data set. The ability to detect and differentiate the decay of ^{135}Xe and the decay of $^{135}Xe^{m}$ has resulted in an improved value of this cross section.]

3 Results and discussion

As indicated above we present the measured cumulative yields and deduced independent yields for the transfer products in Tables 1, 2, 3 and 4. Table 1 contains the data for the lighter projectile-like fragments while Table 2 contains the data for the heavier PLFs. A similar presentation of the data for the TLFs is found in Tables 3 and 4.

3.1 Fragmentation vs. MNT reactions

An oft-cited mantra is that MNT reactions are more effective tools compared to fragmentation reactions for producing very n-rich nuclei near the N = 126 shell closure. The validity of that claim is not obvious. Firstly, the targets for fragmentation reactions are much thicker than the targets used in MNT reaction studies, leading to an enhancement of the production rates of ∼ 2 orders of magnitude in fragmentation reactions.

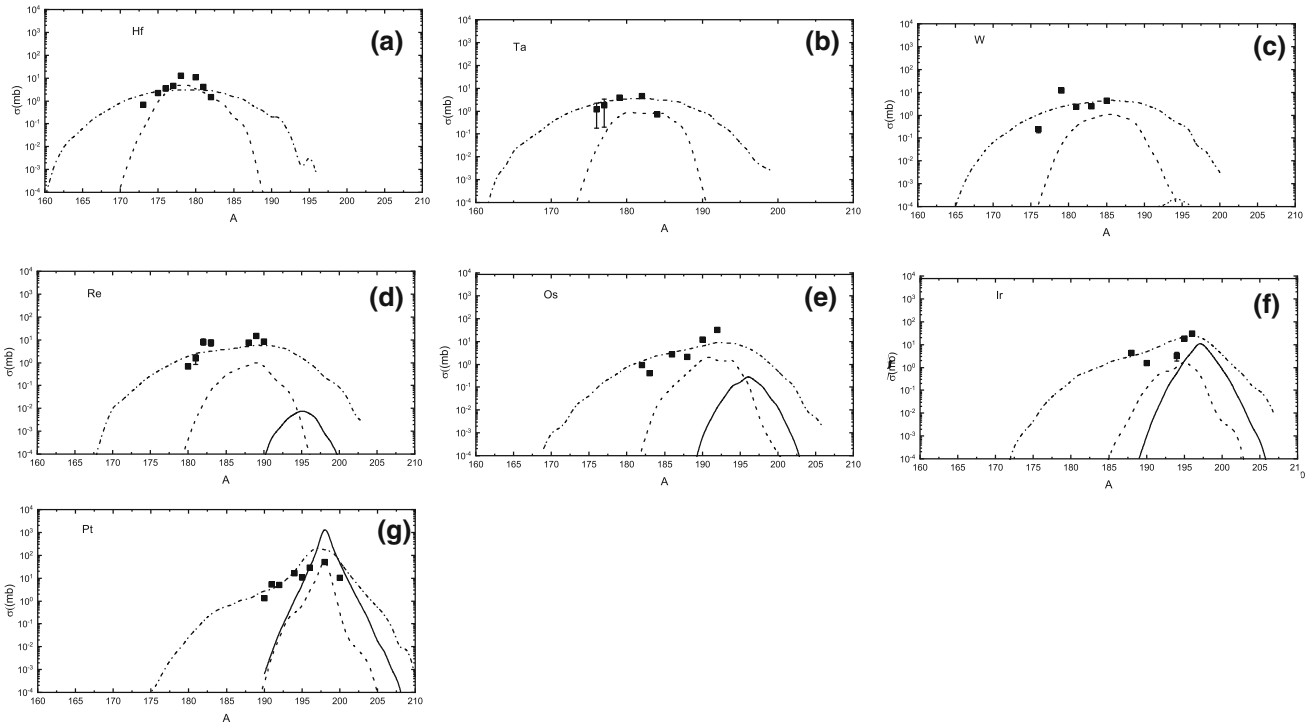

Fig. 1 A comparison of the the predicted (GRAZING-F, DNS and ImQMD) yields and the measured yields of the lower Z TLFs formed in the reaction of 760.5 MeV ^{136}Xe with ^{198}Pt. The solid squares represent the experimental data, while the solid , dashed and the dash-dot lines represent the predictions of the GRAZING-F, DNS and ImQMD models, respectively

A second argument concerns the actual measured production cross sections. In Table 6, we compare the measured yields of the most n-rich products formed in the fragmentation of ^{208}Pb [33], the most n-rich products observed in the reaction of ^{136}Xe with ^{208}Pb [23] and the reaction of ^{136}Xe with ^{198}Pt (this work). (We recognize that the beam energy may not have been the most optimum choice in the work of [23]). In general the comparison of the production cross sections in the cited fragmentation study and the cited MNT study does not reveal a clear-cut advantage for either synthesis technique bearing in mind that fragmentation reactions will not produce significant yields of trans-projectile species while MNT reactions can produce trans-target species.

3.2 The GRAZING-F model

The GRAZING model, in general, suggests that to make neutron-rich nuclei one should use neutron rich projectiles colliding with heavy nuclei (where all stripping and pickup channels are open). (^{136}Xe is a relatively n-rich projectile with N/Z = 1.52.) For each neutron that is transferred, the cross section is predicted to drop by a factor of $\sim$3.5. (sequential transfer) The transfers for the target-like fragments will move the products to higher values of Z but lower values of N. For the projectile-like fragments, the GRAZING model suggests the products will have lower Z and higher values of N. One neutron transfer is expected to be much larger than one proton transfer but pure two proton transfer is expected to be as large as one proton transfer, perhaps. The excitation energy of the primary transfer products is expected to be high, requiring a careful treatment of the fragment de-excitation, hence the GRAZING-F variant. In Figs. 1 and 2, we compare the predictions of the GRAZING-F model with the measured data from this experiment.

The GRAZING-F model described only the yields of the near target isotopes of Hg and Tl ($\Delta Z = +2, +3$), perhaps due to pair transfer. For the $\Delta Z = 0$ transfers (the Pt isotopes), the GRAZING-F model overestimated the cross sections of the near target products and underestimated the yields of the products involving larger transfers ($\Delta Z = 4$–7). That result suggests that the use of the GRAZING model is generally not appropriate for even the smallest transfers.

3.3 The DNS model

The di-nuclear systems (DNS) is intended to treat those MNT reactions in which there is substantial contact between the colliding nuclei, and as such, it complements the GRAZING model which treats peripheral collisions. For the cases shown in Figs. 1 and 2, the DNS model predictions are shown as a

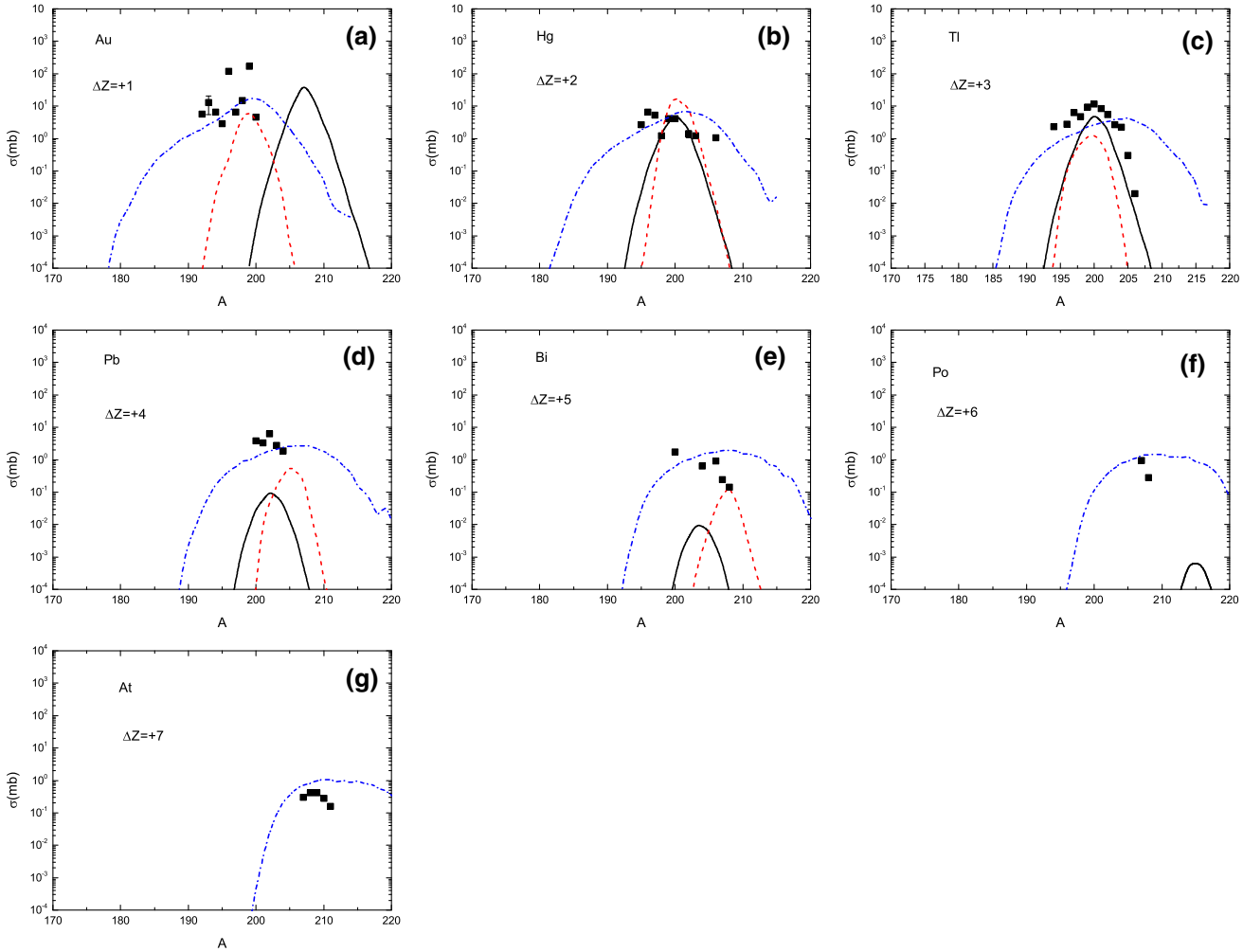

Fig. 2 A comparison of the the predicted (GRAZING-F, DNS and ImQMD) yields and the measured yields of the larger Z TLFs formed in the reaction of 760.5 MeV ^{136}Xe with ^{198}Pt. The solid squares represent the experimental data, while the solid , dashed and the dash-dot lines represent the predictions of the GRAZING-F, DNS and ImQMD models, respectively

red dashed line. For the large transfers from the target, with a negative value of ΔZ, such as the formation of Hf and Ta residues from the Pt target, the DNS model does a reasonable job of describing the measurements. For the smaller negative transfers from the target, the DNS model underestimates the observed cross sections. For the $\Delta Z = 0$ transfers, the DNS model grossly underestimates the observed yields. For the transfers to the target (Fig. 2), the DNS model seriously underestimates the observed transfers, especially those involving a large value of ΔZ. Typically the breadth of the ΔN distribution for a given ΔZ is grossly underestimated.

3.4 The ImQMD model

Based upon prior work [24,34,35], the Improved Quantum Molecular Dynamics (ImQMD) model is expected to give the best overall description of the cross sections in multi-nucleon transfer reaction studies. The data shown in Figs. 1 and 2 support that expectation. For the small and **large** transfers, the ImQMD model describes the observations adequately, even for transfers of seven protons. For future studies of MNT reactions, this model appears to be the best choice for describing the data.

3.5 The optimum projectile energy for the ^{136}Xe +^{198} Pt reaction

Could we have chosen a better energy for the incident beam to optimize the production of n-rich MNT products? Li et al. [16] have examined this question for the ^{136}Xe +^{198} Pt reaction and they concluded that 6.20 MeV/A is the optimum beam energy (E_{lab} = 843 MeV) according to the ImQMD model. Our work used a projectile energy of 760.5 MeV (5.6 MeV/A). For the Z = 74, Z = 76, Z = 78 and Z = 80 products

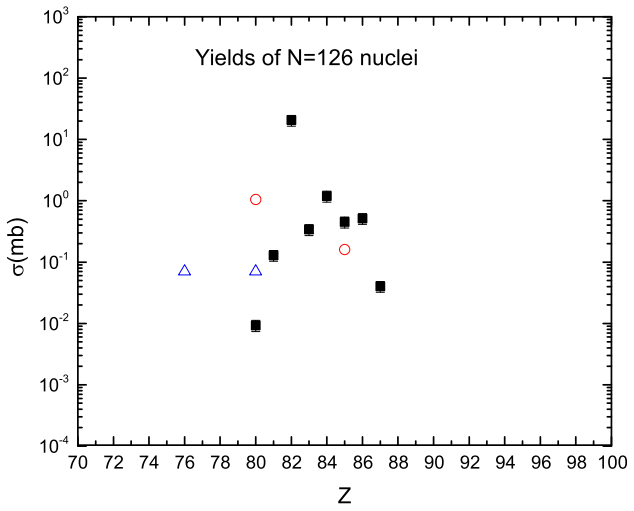

Fig. 3 The yields of N=126 nuclei for this study (open red circles), for the measurements of Barrett [23] (black squares) for the ^{136}Xe +^{208} Pb reaction and for the measurements of [32] (blue triangles)

with N = 126, the predicted [16] change in cross section between projectile energies of 5.25 and 6.20 MeV/A is not significant. For the Z = 82 (Pb) and Z = 84 (Po) products with N = 126, the increase in predicted production cross sections between 5.25 to 6.20 MeV is less than a factor of 5.

3.6 The optimum target for making N =126 nuclei

If we were to try to optimize the production of N=126 nuclei, would another projectile/target combination have been better? According to the DNS model calculations of Zhu et al. [11], the production cross sections of the N=126 nuclei, ^{199}Ta, ^{200}W, ^{201}Re and ^{202}Os, would have increased by about a factor of 1000 if one had used the ^{198}Pt +^{238} U reaction instead of the ^{136}Xe +^{198} Pt reaction.

3.7 The optimum projectile-target-energy combination to make N=126 nuclei

In Fig. 3, we show the measured yields of the N=126 nuclei formed in three reactions, this work (760.5 MeV ^{136}Xe with ^{198}Pt), the work of Watanabe et al. (1085 MeV ^{136}Xe with ^{198}Pt), and the work of Barrett et al. (743 MeV ^{136}Xe with ^{208}Pb.). All the data appear to be roughly consistent with one another, with the greatest number of N=126 nuclei being formed in the 743 MeV ^{136}Xe with ^{208}Pb reaction.

3.8 N/Z regions populated by the MNT reaction of 760.5 MeV ^{136}Xe with ^{208}Pb

The data in Tables 1, 2, 3 and 4 allow us to ask what are the general positions of the MNT products in the N,Z plane. In Fig. 4, we show the yield contours for the PLFs and TLFs .

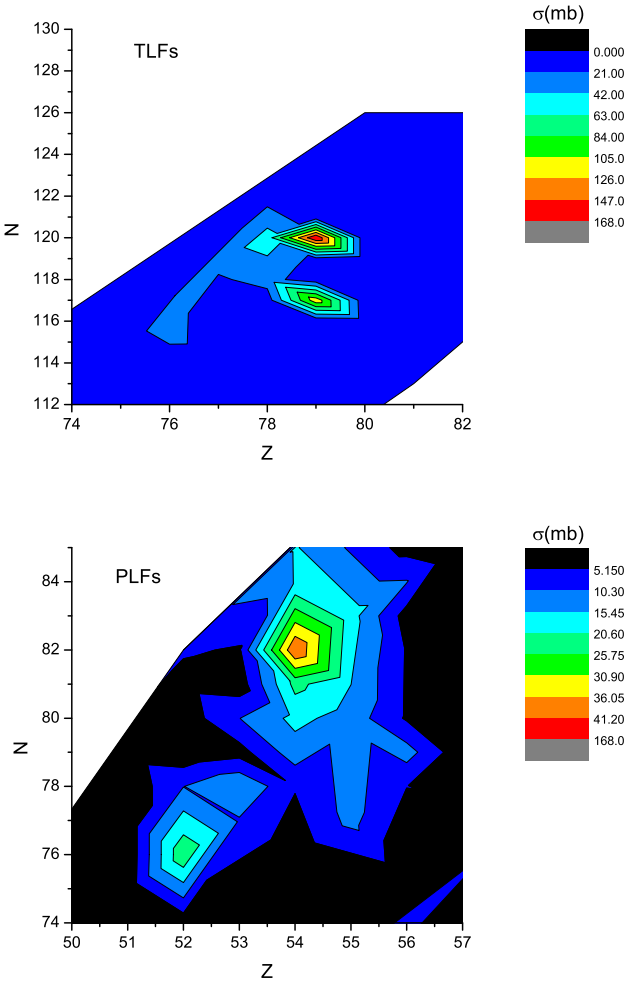

Fig. 4 Contour plots of the measured PLF and TLF distributions from the reaction of 760.5 MeV ^{136}Xe with ^{198}Pt

For the PLFs, the highest yields are seen for the (N,Z) of the projectile (^{136}Xe) , i.e., Z=54 and N=82. There is a secondary peak at Z=52, N=76 ($\Delta Z = -2$, $\Delta N = -6$). One might hope the missing nucleons were transferred to a TLF, but that does not seem to be the case. The principal peak in the (Z,N) yield distribution for the TLFs is at Z=79 ($\Delta Z = +1$), and N=120 ($\Delta N = 0$). These observations are in accord with the predictions of the ImQMD model, but do not seem to have a simple explanation.

3.9 The product mass yield distribution

From the individual nuclidic production cross sections, one can deduce fragment mass distributions, shown in Fig. 5. (The uncertainties in the calculated "independent yield" cross sections deduced using our procedures have been examined by Morrissey et al. [36] and they found a systematic uncertainty of ± 30% associated with our procedures.) For the PLFs, two broad peaks are observed in the fragment mass

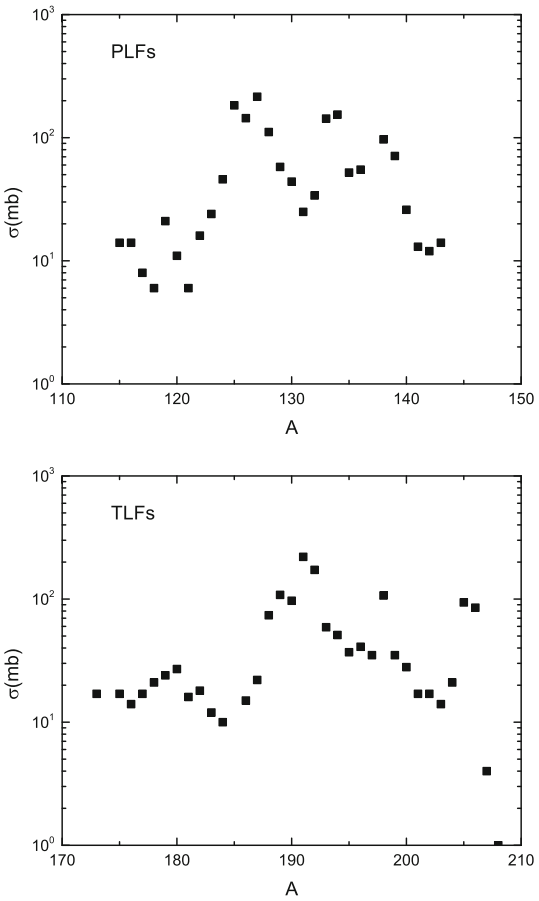

Fig. 5 Smoothed plots of the measured PLF and TLF distributions from the reaction of 760.5 MeV ^{136}Xe with ^{198}Pt

distributions, at A=126–128 and A $\sim$ 136. The latter peak presumably reflects the mass of the projectile, while the former peak at A $\sim$ 126–128 is consistent with the data in Fig. 4, which shows a second PLF peak at Z = 52, N = 76. This peak corresponds to a transfer from the projectile of 2 protons and 6 neutrons (after de-excitation). The transfer of two protons presumably reflects the enhancement of pair transfer. The n/p ratio for the transferred nucleons is $\sim$ 3, reflecting the efficacy of MNT processes in forming n-rich nuclei.

For the TLFs, one observes peaks at A $\sim$ 190, 198 and 206. The peak at A $\sim$ 198 presumably reflects quasi-elastic transfer from the ^{198}Pt target. This peak also corresponds to the peak in the TLF contour plot at Z=79, N=117 (A $\sim$ 196). The peak at A $\sim$ 206, presumably reflects the complement of the ΔZ = -2, ΔN = -6 transfer seen for the PLFs. The origin of the peak at A $\sim$ 190 is not clear.

3.10 Comparison with experiment of Watanabe et al.

As mentioned previously Watanabe et al [32] studied the reaction of $E_{c.m.}$ = 643 MeV ^{136}Xe +^{198} Pt. They reported the yields of several PLFs and two TLFs, Os and Hg. Karpov and Saito [20] compared these results with Langevin model calculations, finding excellent agreement between the measurements and the calculations. Karpov and Saito pointed out, based upon their calculations that the most neutron-rich nuclei were the result of collisions with low total kinetic energy loss (TKEL), a conclusion in agreement with suggestions of [32]. These low TKEL events correspond to peripheral collisions. It would be useful to have data that measures the yields of trans-target MNT products as a function of angle of emission to better understand the optimal conditions for the production of n-rich nuclei, especially those near the N = 126 shell.

4 Conclusions

What have we learned from this experiment? We found : (a) a complete, integrated picture of the yields of the target-like and projectile-like fragments from a typical MNT reaction, 760 MeV ^{136}Xe +^{198} Pt. (b) that only the ImQMD model correctly described the production cross section data. (The GRAZING and DNS models had shortcomings in describing the data). (c) for the reactions, 760 MeV ^{136}Xe +^{198} Pt, 743 MeV ^{136}Xe +^{208} Pb and 1085 MeV ^{136}Xe +^{198} Pt, the yields of the N=126 nuclei were the highest and most extensive for the 743 MeV ^{136}Xe +^{208} Pb reaction. (d) the disadvantage of producing N=126 nuclei by fragmentation (rela- tive to MNT reactions) was not obvious (e) some prominent MNT transfer channels, such as the observed two proton, six neutron transfer from the ^{136}Xe projectile to the ^{198}Pt target, involve complex mechanisms (f) further detailed measurements of the kinematics of the MNT reactions leading to the production of N=126 nuclei are needed.

Acknowledgements This material is based upon work supported in part by the U.S. Department of Energy, Office of Science, Office of Nuclear Physics under award numbers DE-FG06-97ER41026 (OSU), DE-FG02-97ER41041 (UNC), DE-FG02-97ER41033 (TUNL), DE-FG02-94ER40848 (UMassLowell) and contract number DE-AC02-06CH11357 (ANL). This research used resources of ANL's ATLAS facility, which is a DOE Office of Science User facility.

Author contributions All the authors were involved in the preparation of the manuscript. All the authors have read and approved the final manuscript. We wish to thank Prof. Feng-Shou Zhang and his associates for making the DNS and ImQMD calculations cited in this paper. We thank Dr. A. Chemey for helping us with some computational issues.

Data Availability Statement This manuscript has associated data in a data repository. [Authors' comment: The data that support the findings of this study are available from the corresponding author upon reasonable request.]

References

1. J.V. Kratz, W. Loveland, K.J. Moody, Nucl. Phys. A **944**, 117 (2015)
2. F.-S. Zhang, C. Li, L. Zhu, P. Wen, Front. Phys. **13**, 132113 (2018)
3. W. Loveland, Front. Phys. **7**, 23 (2019)
4. http://personalpages.to.infn.it/~nanni/grazing/
5. A. Winther, Nucl. Phys. A **572**, 191 (1994)
6. A. Winther, Nucl. Phys. A **594**, 203 (1995)
7. L. Corradi, G. Pollorolo, S. Szilner, J. Phys. G Nucl. Part. Phys. **36**, 113101 (2009)
8. R. Yanez, W. Loveland, Phys. Rev. C **91**, 044608 (2015)
9. G.G. Adamian, N.V. Antonenko, W. Schied, Phys. Rev. C **68**, 034601 (2003)
10. L. Zhu, Z.-Q. Feng, F.-S. Zhang, J. Phys. G Nucl. Part. Phys. **42**, 085102 (2015)
11. L. Zhu, Jun-Su, W.-J. Xie, F.S. Zhang, Phys. Lett. B **767**, 437 (2017)
12. K. Zhao, Z. Li, W. Xizhen, Y. Zhang, Phys. Rev. C **88**, 044605 (2013)
13. C. Li, P. Wen, J. Li, G. Zhang, B. Li, X. Xinxin, Z. Liu, S. Zhu, F.-S. Zhang, Phys. Lett. B **776**, 278 (2018)
14. L. Zhu, C. Li, S. Jun, C.-C. Guo, W. Hua, Phys. Lett. B **791**, 20 (2019)
15. G. Zhang, C.A.T. Sokhna, Z. Liu, F.-S. Zhang, Phys. Rev. C **100**, 024613 (2019)
16. C. Li et al., Phys. Rev. C **99**, 024602 (2019)
17. V. Zagrebaev, W. Greiner, J. Phys. G Nucl. Part. Phys. **35**, 125103 (2008)
18. V.I. Zagrebaev, W. Greiner, Yuanzihe Wuli Pinglun **32**, 137 (2015)
19. A. Karpov, V. Saiko, EPJ Web Conf. **163**, 00027 (2017)
20. A.V. Karpov, V.V. Saiko, Phys. Rev. C **96**, 024618 (2017)
21. V.V. Saiko, A.V. Karpov, Phys. Rev. C **99**, 014613 (2019)
22. E.M. Kozulin, G.N. Knyazheva, I.M. Itkis, N.T. Kozulina, T.A. Loktev, K.V. Novikov, I. Harca, J. Phys. G Conf. Ser. **515**, 012010 (2014)
23. J.S. Barrett et al., Phys. Rev. C **91**, 064615 (2015)
24. V.V. Desai et al., Phys. Rev. C **99**, 044604 (2019)
25. http://www.calel.org/range.html
26. J. Spenser Barrett, Ph. D. thesis. Oregon State University (2015)
27. LISE++, version 10.1.94, spectrometric calculator of J. Kantele
28. http://radware.phy.ornl.gov/
29. J.F.C. Cocks et al., J. Phys. G **26**, 23 (2000)
30. J.F.C. Cocks et al., Nucl. Phys. A **645**, 61 (1999)
31. G. Friedlander, J.W. Kennedy, J.M. Miller, E. Macias, *Nuclear and Radiochemistry*, 3rd edn. (Wiley, New York, 1981)
32. Y.X. Watanabe et al., Phys. Rev. Lett. **115**, 172503 (2015)
33. T. Kurtukian-Nieto et al., Phys. Rev. C **89**, 024616 (2014)
34. T. Welsh et al., Phys. Lett. B **771**, 119 (2017)
35. V.V. Desai et al., Phys. Rev. C **101**, 034612 (2020)
36. D.J. Morrissey, W. Loveland, M. de Saint-Simon, G.T. Seaborg, Phys. Rev. C **21**, 1783 (1980)